1 # Title: Dunes on Pluto

2 **Authors:** Matt W. Telfer[1]*[†], Eric J.R. Parteli[2][†], Jani Radebaugh[3][†], Ross A. Beyer[4,5], Tanguy

3 Bertrand[6], François Forget[6], Francis Nimmo[7], Will M. Grundy[8], Jeffrey M. Moore[5], S. Alan

4 Stern[9], John Spencer[9], Tod R. Lauer[10], Alissa M. Earle[11], Richard P. Binzel[11], Hal A. Weaver[12],

5 Cathy B. Olkin[12], Leslie A. Young[9], Kimberley Ennico[5], Kirby Runyon[12], and The New

6 Horizons Geology, Geophysics and Imaging Science Theme Team[‡]

7 **Affiliations:**

8 1. School of Geography, Earth and Environmental Sciences, Plymouth University, Drake Circus,

9 Plymouth, Devon, UK, PL4 8AA.

10 2. Department of Geosciences, University of Cologne, Pohligstraße 3, 50969 Cologne, Germany.

11 3. Department of Geological Sciences, College of Physical and Mathematical Sciences, Brigham

12 Young University, Provo, Utah, UT 84602, USA.

13 4. Sagan Center at the SETI Institute, Mountain View, CA 94043, USA.

14 5. NASA Ames Research Center, Moffett Field, CA 94035, USA.

15 6. Laboratoire de Météorologie Dynamique, Université Pierre et Marie Curie, Paris, France.

16 7. University of California Santa Cruz, Santa Cruz, CA, USA.

17 8. Lowell Observatory, Flagstaff, AZ, USA.

18 9. Southwest Research Institute, Boulder, CO, USA.

19 10. National Optical Astronomy Observatory, Tucson, AZ 85726, USA.

20   11. Department of Earth, Atmosphere, and Planetary Science, Massachusetts Institute of

21   Technology, Cambridge, MA 02139, USA.

22   12. Johns Hopkins University Applied Physics Laboratory, Laurel, MD, USA.

23   † These authors contributed equally to this work.

24   * Correspondence to: matt.telfer@plymouth.ac.uk

25   ‡ The list of team members is provided in the supplementary material

26

27   **Abstract**: The surface of Pluto is more geologically diverse and dynamic than had been

28   expected, but the role of its tenuous atmosphere in shaping the landscape remains unclear. We

29   describe observations of regularly spaced, linear ridges from the New Horizons spacecraft whose

30   morphology, distribution and orientation are consistent with being transverse dunes. These are

31   located close to mountainous regions and are orthogonal to nearby wind streaks. We demonstrate

32   that the wavelength of the dunes ($\sim 0.4 - 1$ km) is best explained by the deposition of sand-sized

33   ($\sim$200-$\sim$300 μm) particles of methane ice in moderate winds (<10 m s^{-1}). The undisturbed

34   morphology of the dunes, and relationships with the underlying convective glacial ice, imply that

35   the dunes have formed in the very recent geological past.

36   **One Sentence Summary:**

37   We describe dune-like landforms on Pluto, which likely result from granular solids affected by

38   the wind regime at the margin of an icecap and mountains.

39

40

Main Text:

Dunes require a supply of particulate material on a surface and a fluid boundary layer to entrain the grains (i.e. wind, for dunes on a planet's surface). They have been identified in some surprising locations: Contrary to predictions (*1*), Saturn's moon Titan has a broad belt of linear dunes encircling its equatorial latitudes (*2*), and despite the lack of a persistent atmosphere, eolian landforms (i.e. those related to wind) have also been suggested to occur on comet 67P/Churyumov-Gerasimenko (*3*). On July 14 2015, NASA's New Horizons spacecraft flew past Pluto, which provided spectral data and imagery of the surface at resolutions as detailed as 80 m/pixel (*4*). The combination of Pluto's low gravity (0.62 m s^{-1}, or 1/12th that of Earth), sparse atmosphere [1 Pa *(5)*], extreme cold [~ 45 K *(5)*] and surface composition [N_2, CO, H_2O and CH_4 ices *(6)*]] made pre-encounter predictions of surface processes challenging. However, pre-encounter speculation included that eolian processes, and potentially dunes, might be found on Pluto (*7*), because, despite the relatively thin atmosphere, the winds could possibly sustain saltation (i.e. particle movement by ballistic hops) in the current surface conditions. We examined images from the Long Range Reconnaissance Imager (LORRI) instrument (*8*) on New Horizons, taken during the probe's closest approach to Pluto, to search for landforms with the morphological and distributional characteristics of dunes. We also searched spectroscopic data from the Multispectral Visible Imaging Camera [MVIC *(9)*] for evidence of sufficient sand-sized ice particles to form dunes, and discuss how sublimation may play a role in lofting these particles enabling them to be saltated into dunes.

63 **Observations from New Horizons**

64 The surface of Pluto, as revealed by New Horizons, is diverse in its range of landforms,

65 composition and age (*4, 10*). One of the largest features, Sputnik Planitia (SP), is a plain of N_2,

66 CO and CH_4 ice (*6* and Fig. S1) that extends across Pluto's tropics and at its widest point covers

67 30° of longitude (Fig. 1A). Polygonal features on the surface of SP, tens of kilometers across and

68 bounded by trenches up to 100 m deep (Fig. 1B and 1C), have been interpreted as the result of

69 thermally-driven, convective overturning of the ice (*11,12*), which, together with the uncratered

70 surface of SP (*4*), suggests a geologically young (<500 ka; *11,12*) and active surface. Much of

71 the western edge of the ice is bounded by the Al-Idrisi Montes (AIM), a mountainous region

72 with relief of up to 5 km. On the SP plain bordering these mountains, distinct, regularly spaced,

73 linear ridges are evident within a belt of approximately 75 km from the mountain margin (Fig

74 2A). They have positive relief as evident from shadows consistent with the mountains. The

75 ridges show pronounced spatial regularity (~0.4 - 1 km wavelength), substantial length/width

76 ratios (sometimes >20 km length), consistent shape along these lengths, and the presence of

77 merging/bifurcation junctions (Fig. 1C and 1D; Fig. 2D and 2E). These junctions are

78 approximately evenly spread between 47 north-facing bifurcations and 42 south-facing splits,

79 and there is no clear spatial patterning to the direction of junctions. Farther from the mountain

80 margin, toward the southeast, the ridges become more widely spaced and generally larger, while

81 still in isolated fields or patches. Dark streaks are also found across the surface of the ice,

82 typically behind topographic obstacles, and have been interpreted as wind streaks (*4*). These

83 features indicate there are loose particles near and on the surface, as the streaks are thought to

84 result from the deposition of suspended, fine particles in the lee of obstacles to wind flow (*4, 5,*

85 *13*; Fig. 1C, 1E).

86   We have identified 357 pale-colored, linear ridges on SP adjacent to the AIM (Fig. 2A, 2B, 2C),

87   as well as six darker wind streaks in addition to the seven previously identified (4). The ridges

88   closest to the SP/AIM mountain front are oriented approximately parallel with it, and ridges

89   farther to the southeast shift orientation clockwise by ~30° over a distance of ~75 km (Fig. 2A

90   and 2B); the ridges farther from the SP/AIM margin are significantly *(Mann-Whitney U = -7.41;*

91   *p < 0.0001)* more widely spaced (Fig. 2C). Beyond the ~75 km-wide belt in which the linear

92   ridges are predominantly found, the morphology of the surface changes, with preferential

93   alignment of the ridges gradually disappearing (Fig. S2), until the landscape is dominated by

94   weakly- or un-aligned, but still regularly dispersed, pits likely caused by sublimation of the ice

95   (*14*). Wind streaks adjacent to the SP/AIM border are perpendicular to the ridges and mimic the

96   shift in orientation shown by the ridges (Fig. 3A, 3B). Streaks within the zone in which the

97   ridges are found (i.e. < 75 km from the SP/AIM border) are geographically (i.e. clockwise from

98   north) oriented 113 ± 4° (1 standard deviation,σ, with sample number,n=4), whilst more distant

99   wind streaks are oriented significantly [(*heteroscedastic Student's t = 9.912; p < 0.001* (Fig.

100   3B)] differently at 153 ± 10° (1σ, n=9).

101   **Interpretation as dunes**

102   The ridges found on western SP have morphological similarities to dunes (Figs. 1C, 1D,

103   4A, 4B and 4C). In addition to analogue similarities, we argue that these landforms are most

104   consistent with an initial eolian depositional origin (i.e. dunes) on the grounds that: (a) a

105   depositional origin is favored by the superimposition of many of the dunes on the trenches

106   bordering SP's convective cells (Figs. 1D, 2D and 2E), (b) the distribution of the dunes with

107   pattern coarsening (enlarging toward the southeast), away from the mountains (Fig. 4C), which is

108   characteristic of dunefields; (c) their orientation, and systematic regional changes to this

109   orientation, are more readily explained by the wind regime than variations in incoming solar

110   radiation; (d) the presence of pronounced wind streaks, orthogonal to the dunes, demonstrates the

111   potential efficacy of Pluto's winds; (e) their location, on a methane- and nitrogen-dominated ice

112   cap adjacent to mountains, is where the strongest winds and a supply of sediment might be

113   expected, and; (f) their differing morphologies and undeformed regular alignment differs from

114   the randomly aligned, shallow pits that border on the dune regions of SP (Fig. 4E and S2), and

115   the deeply incised, discrete, aligned pits that can be found towards SP's southern and eastern

116   margins (Fig. 4D). These pit-like features are morphologically distinct from the dune-like ridges

117   farther north near the AIM that we discuss here (Figs. 4A and D). To test this hypothesis, we use

118   a model (*15*) to examine the saltation of sand-sized (in this case, ~200-300 μm) particles on

119   Pluto. Once initiated, the model indicates that saltation can be sustained even under the low

120   (Earth-like; 1-10 m s^{-1}) wind speeds predicted at the surface today (*16*). However, the model also

121   suggests that an additional process may be necessary to initially loft particles (*15*). This can be

122   accomplished by sublimation, which is capable of lofting particles, and we model this process to

123   find that particles can be entrained. This function of sublimation is in addition to the role

124   sublimation may play in eroding mature dunes to more altered forms, which is also discussed in

125   more detail below. Thus, under the current conditions, if there are sufficiently non-cohesive

126   sand-sized particulates on the surface of Pluto, we should expect to find dunes.

127   Terrestrial and planetary dunes that form straight ridges can occur either perpendicular to the

128   wind, forming transverse dunes, or parallel to the net local wind regime, forming longitudinal (or

129   linear) dunes, and regional variation in the alignment of such dunes on earth is typically

130   associated with meso or large scale atmospheric patterns (*17*). Wind streaks are well known on

131   Venus and Mars, are present even under the tenuous atmosphere of Triton, and are generally

132   considered to represent the wind direction (*13*). The presence of pronounced wind streaks (Fig.

133   1C) within the dunefield, very nearly orthogonal to the dune trends, suggests that the observed

134   dunes are transverse forms (Fig. 3A). The transverse nature of the dunes is further supported by

135   the lack of consistency in bifurcation orientation; within dunefields oriented parallel to net

136   sediment-transporting winds, such defects tend to cluster in terms of their orientation (*18*). The

137   transverse orientation also shows that these ridges cannot be sastrugi (erosional snow ridges that

138   form parallel to net winds) (*19*), or other erosional features analogous to yardangs (wind-carved

139   ridges). The dunes in the northwestern portion of SP/AIM (Fig. 4A) are even more regularly

140   spaced and parallel than many transverse dunes on Earth. Possible explanations for this include a

141   highly consistent wind regime, lack of topographic deflection of winds, or a smooth substrate.

142   **Conditions for the formation of dunes and sublimation pits**

143   The existence of dunes on the surface of Pluto requires three necessary criteria to be met. Firstly,

144   there must be a fluid atmosphere of sufficient density to make eolian transport possible.

145   Secondly, there must be a granular material of a size and density, and with sufficiently low

146   cohesion, that it can be entrained by winds. On Earth, this role is typically played by sand-sized

147   mineral grains of a variety of compositions, including snow and ice. Thirdly, given the high wind

148   speeds needed to lift surface particles against cohesion forces (*20*; Fig. 5), a specific mechanism

149   must exist to loft large quantities of ice particles into the atmosphere where they are available for

150   eolian transport. The presence of these criteria alone is necessary but not sufficient to identify the

151   surface features as dunes. To justify our interpretation of these features as being dunes we also

152   examine the conditions required for the other most likely candidate: aligned sublimation pits.

153   *Winds*

154   The orientations of the dunes and the wind streaks change locally, and consistently; in the case of

155   the dunes, over a distance on the order of $10\text{-}10^2$ km. This implies that the topography and/or

156   surface composition has influenced the local wind regime, as was anticipated (*21*). These

157   orientations are consistent with sublimation-driven and topographic mechanisms for the

158   horizontal displacement of the atmosphere, as winds are generated by a gravity-driven flow

159   towards lower regions. Modeling of Pluto's current atmosphere suggests that surface winds on

160   the order of $1\text{-}10$ ms^{-1} are possible; they should be strongest where there are topographic

161   gradients and when driven by sublimation of surface ices by sunlight (*15*). The location of the

162   dunes at the western margins of the SP and AIM should thus be amongst the windiest locations

163   on the known regions of Pluto. As with Earth and Mars, once grain transport along the surface of

164   Pluto has begun, increased efficacy of grain-splash (the ejection of new particles due to grains in

165   saltation colliding with the ground) promotes a hysteretic effect that further sustains sediment

166   flux (*22, 23*). We use a numerical model (*15*) to demonstrate that despite the high wind speeds

167   needed for initial eolian entrainment, eolian transport can, once established, be sustained with

168   wind speeds of ~ 10 m s^{-1} (Fig. 5).

169   *Sediment supply*

170   Although terrestrial dunes are typically associated with quartz, basalt or gypsum sand, other

171   materials can form the grains for dune development. Snow dunes of a very large scale are

172   observed in the center of the Antarctic continent (*24*); on Titan, it is generally assumed to be

173   atmosphere-derived organics, perhaps initially tholins, which form the equatorial belt of giant

174   dunes (*25*). While tholins are thought to form the dark patches of Pluto's equatorial regions (*6*),

175   the dunes evident on SP are light in color and are thus not formed from the same complex,

176   organic, photochemically-derived haze seen in Pluto's atmosphere (*4*). The most likely

177   candidates are thus N_2 and CH_4 ices. The surface of SP has generally been interpreted as

178   predominantly composed of N_2 ice (*4, 5*), just as solidified nitrogen snows are believed to

179   account for Triton's ice-covered surface (*26, 27*). The zone in which the ridges occur is

180   coincident with the latitudes in which net N_2 condensation occurs over the course of a Pluto year

181   (*16*; Fig. S3). However, recent analyses suggest that the composition may be a more complex

182   mix of N_2, CH_4 and CO ices (*29*). Our analysis of data from the MVIC instrument, using a CH_4

183   filter (*15*) suggests that the location of the ridges and streaks coincides with a region of enhanced

184   CH_4 ice content (Fig. S4). To the west of SP, the Enrique Montes in Cthulhu Macula (CM) have

185   been shown to be capped with methane, presumably as the result of condensation or precipitation

186   (*29, 30*). CH_4 ice retains hardness and rigidity under Pluto surface conditions, which is ideal for

187   saltation and dune formation, while N_2 ice is likely to be softer. These constraints lead us to

188   conclude that the dunes are formed predominantly of grains of methane ice, though we do not

189   rule out that there could also be a nitrogen ice component. The presence of transverse forms,

190   indicating sediment-rich local conditions, as opposed to more sediment-starved isolated barchans

191   (discrete, crescentic dunes), suggests that locally, the sediment supply to this region of SP must

192   be, or have been, abundant. Given the strength of the color and boundary delineations of methane

193   in the AIM (Fig. S3), the methane ice may be quite thick and perhaps similar to valley glaciers in

194   these isolated regions. If such high-altitude methane snowpack is a regular, seasonal occurrence,

195   this may be a substantial reservoir from which to derive the abundant sand across the

196   northwestern surface of SP required to form these transverse dunes.

197   *Grain size*

198   Credible sediment sizes are required for dune formation under the likely eolian regime. The grain

199   sizes proposed for nitrogen ices (e.g., on Triton) have varied from micrometer (*31, 32*) to meter-

200   scale (*33*). We develop a method (*15*) to approximately constrain average grain size (*d*) and

201   formative wind speed (*U*), from the mean crest-to-crest distance, or wavelength (λ), of the

202   transverse dunes. For eolian dunes, the relevant length scale controlling this wavelength is the

203   saturation length (L_{sat}) of the sediment flux, which is the distance needed by the flux to adapt to a

204   change in local flow conditions. By combining theory (*34*), which predicts L_{sat} as a function of

205   wind speed and attributes of sediment and atmosphere, with a mathematical model (*35*) for λ as a

206   function of L_{sat} and *U*, we obtain the values of *d* and *U* that are consistent with λ. These values

207   are shown in Fig. S5, for $\lambda \approx 700$ m and $\lambda \approx 560$ m, which correspond to the transverse dunes far

208   from and near to the mountainous area of Fig. 1, respectively. Given that expected formative

209   wind speeds on Pluto are not larger than 10 m s^{-1} (*16*), Fig S5 implies that grain size does not

210   exceed ~370 μm and is most probably in the range between 210 and 310 μm. The spectral

211   response of the MVIC CH$_4$ filter offers an additional constraint on the possible grain sizes

212   observed, as Hapke modelling of the scattering within a granular medium provides a grain-size

213   dependent control on the equivalent width of the absorption band. We find (*15*) that the observed

214   response is consistent with a granular medium of ~200-300 μm.

215   *Lofting*

216   Although eolian transport can be maintained under Pluto's current wind regime, the speeds

217   necessary for initial entrainment are orders of magnitude greater than those believed to be

218   present at Pluto's surface (Fig. 5). An additional process is thus likely to be necessary to initiate

219   eolian activity. In Sputnik Planitia, this process may be related to the intense, solar-driven

220   sublimation of surface ices that injects more than 10^3 m^3 m^{-2} of gas in the atmosphere every

221   afternoon (*16*, their figure 8). When sunlight penetrates through the upper layers of semi-

222   transparent ice particles are lofted, sometimes at high vertical velocities, due to a mechanism

223   often referred to as a solid-state greenhouse (*36*). Therefore, initial entrainment of ice grains that

224   eventually form dunes may result from sublimating subsurface ice, as has been observed in the

225   thin atmospheres of Mars' northern polar region (*37*), and proposed for comet 67P/Churyamov-

226   Gerasimenko (*38,39*) and Triton (24,25). Modeling (*15*) suggests that subsurface N_2 sublimation

227   under Pluto surface conditions is capable of lofting even the densest candidate particles [N_2 ice, at

228   1030 kg m^{-3}, is denser than CH_4 ice, at 494 kg m^{-3} (*40*)] with sizes ~200 μm, even at 0.1 Pa;

229   within the range of both Pluto's atmospheric pressure and the solid N_2 vapor pressure. Surface

230   ices of mixed composition offer an additional potential mechanism for facilitating grain lofting.

231   At the nitrogen frost point temperature of 63 K (*11*), pure methane ice particles mixed with

232   nitrogen should not sublimate at all. As methane particles are slightly heated by the sun, they

233   should enable the sublimation of the nitrogen ice that they touch and thus be readily lofted into

234   the atmosphere. Similar processes have recently been suggested for the migration of tholin

235   deposits on the surface of Pluto (*41*). Past periods of higher atmospheric pressures, which have

236   been suggested (*42*), could facilitate initial entrainment due to increased efficacy of eolian

237   processes.

238   *Sublimation*

239   The landscape of SP contains evidence of sublimation-driven landforms (*4, 7, 14*), and this

240   process is important in shaping parts of Pluto's surface. We consider whether the landforms

241   described here are more consistent with origins attributable to eolian or sublimation processes.

242   Locally, sublimation pits are deeply incised and may align to form linear troughs up to 10s of km

243   long and up to ~1 km deep (*4, 7*). Frequently, and especially towards the southern and eastern

244   margins of SP, any alignment is subsequently heavily deformed, presumably driven by glacial

245   flow and convective overturning. Analogue landforms on Earth are provided by sublimation-

246   driven textures of snow and ice surfaces: ablation hollows (suncups) and penitentes (*14, 43*). On

247   Earth, ablation hollows on snow may become aligned to leave ridges (penitentes), which align

248   themselves to within ±30° of east-west (i.e. the annual mean net sun path (*44*). Although the

249   orientation of any penitentes on Pluto is likely to be more complex and seasonally dependent,

250   they are only likely to form wavelengths in excess of ~1000 m (*45*). It is possible that

251   sublimation has acted upon already formed dunes in some regions (Fig. 2A). In polar regions on

252   Earth, wind-driven snow or ice grains can produce dunes, which then become hardened by

253   sintering and begin to undergo modification by wind and sublimation processes, thus changing

254   from depositional to erosional landforms (*44, 45*). Given the tendency of ices to sinter together

255   under the right conditions, this could also happen in the CH_4 or N_2 ices of Pluto's dunes.

256   Sublimation erosion of Pluto's dunes may enlarge and round the areas between the dunes, and

257   sharpen the dune crests while preserving the overall dune orientation and spacing. This

258   morphology may be seen just at the resolution limit in the features farthest from the mountains in

259   Fig. 2a (enlarged view in Fig. S2). This is supported by modeling (*15*) of the net accumulation of

260   ices across Pluto's surface during the past two (Earth) centuries (Fig. S4), which suggests that for

261   the past ~30 Earth years, the dunefield has been experiencing net sublimation. Some of these

262   features may have progressed so far towards being erosional that we have not identified them as

263   dunes (Fig. S2).

264   *Age*

265   An upper limit on the age of the dunes, which sit atop the ice of the western margins of SP, is

266   imposed by the recycling rate of the upper surface of the convectional cells within the ice (i.e. <

267   500 ka) (*11, 12*). This overturning of the substrate, inferred from the complete absence of

268   identified craters on SP, provides an age constraint for superficial landforms which is not

269   available for dunes on other solar system bodies, and implies a geologically and/or

270   geomorphologically active surface (*4, 10, 46*). Surface features, undistorted by the convectional

271   overturning within the ice, must be much younger than the timescales of convection, therefore

272   closer to the timescales of Pluto's strong seasons (i.e. terrestrial decades – centuries). Further

273   evidence that the dunes form on a timescale substantially shorter than that of the convection is

274   suggested by the superposition of the dunes over the depressions at the cell margins (Fig. 1G).

275   **Summary and Conclusions**

276   We have presented evidence that the highlands adjacent to SP accumulate methane. The ridged,

277   dune-like landforms nearby, and accompanying wind streaks, are rich in methane relative to their

278   underlying substrate. Although the wind speeds needed for eolian entrainment are higher than the

279   likely wind speeds present on the surface, sublimation provides a credible mechanism for lofting

280   grains. Numerical sediment transport and spectral modeling suggest these methane grains are

281   approximately 200-300 μm. Our models suggest eolian transport is highly effective under Pluto

282   surface conditions once initiated. An ample sediment supply appears to be available from a

283   seasonally abundant snowpack in the adjacent mountains. The result is the formation of

284   transverse dunes, as we identify in the images from New Horizons. The orientation of the dunes

285   perpendicular to the wind is supported by the local topography and surface, and accompanying

286   wind streaks. The presence of these dunes indicates an active atmosphere that produces

287   geologically young landforms.

288

289

References:

1.   Lorenz RD, Lunine JI, Grier JA, Fisher MA. Prediction of aeolian features on planets: Application to Titan paleoclimatology. Journal of Geophysical Research-Planets. 1995;100(E12):26377-86.

2.   Lorenz RD, Wall S, Radebaugh J, Boubin G, Reffet E, Janssen M, et al. The sand seas of Titan: Cassini RADAR observations of longitudinal dunes. Science. 2006;312(5774):724-7.

3.   Thomas N, Sierks H, Barbieri C, Lamy PL, Rodrigo R, Rickman H, et al. The morphological diversity of comet 67P/Churyumov-Gerasimenko. Science. 2015;347(6220).

4.   Stern SA, Bagenal F, Ennico K, Gladstone GR, Grundy WM, McKinnon WB, et al. The Pluto system: Initial results from its exploration by New Horizons. Science. 2015;350(6258), aad1815.

5.   Gladstone GR, Stern SA, Ennico K, Olkin CB, Weaver HA, Young LA, et al. The atmosphere of Pluto as observed by New Horizons. Science (New York, NY). 2016;351(6279):aad8866.

6.   Grundy WM, Binzel RP, Buratti BJ, Cook JC, Cruikshank DP, Ore CMD, et al. Surface compositions across Pluto and Charon. Science. 2016;351(6279): aad9189.

7.   Moore JM, Howard AD, Schenk PM, McKinnon WB, Pappalardo RT, Ewing RC, et al. Geology before Pluto: Pre-encounter considerations. Icarus. 2015;246:65-81.

8.   Cheng AF, Weaver HA, Conard SJ, Morgan MF, Barnouin-Jha O, Boldt JD, et al. Long-Range Reconnaissance Imager on New Horizons. Space Science Reviews. 2008; 140(1):189-215

9.   Reuter DC, Stern AS, Scherrer J, Jennings DE, Baer JW, Hanley J, et al. Ralph: A Visible/Infrared Imager for the New Horizons Pluto/Kuiper Belt Mission. Space Science Reviews. 2008; 140(1):129-15410.   Moore JM, McKinnon WB, Spencer JR, Howard AD, Schenk PM, Beyer RA, et al. The geology of Pluto and Charon through the eyes of New Horizons. Science. 2016;351(6279):1284-93.

11.   McKinnon WB, Nimmo F, Wong T, Schenk PM, White OL, Roberts JH, et al. Convection in a volatile nitrogen-ice-rich layer drives Pluto's geological vigour. Nature. 2016;534(7605):82-+.

12.   Trowbridge AJ, Melosh HJ, Steckloff JK, Freed AM. Vigorous convection as the explanation for Pluto's polygonal terrain. Nature. 2016;534(7605):79-+.

13.   Sagan, C., Chyba, C. Triton's streaks as windblown dust. Nature. 1990; 346: 546 – 548.

317   14.   Moore JM, Howard AD, Umurhan OM, White OL, Schenk PM, Beyer RA, et al. Sublimation as a

318   landform-shaping process on Pluto. Icarus. 2017; 287: 320-333

319   15.   Materials and methods are available as supplementary materials on Science Online.

320   16.   Forget F, Bertrand T, Vangvichith M, Leconte J, Millour E, Lellouch E. A post-new horizons global

321   climate model of Pluto including the N2, CH4 and CO cycles. Icarus. 2017; 287: 54-71.

322   17.   Bagnold RA. The physics of blown sand and desert dunes. London: Chapman and Hall; 1941. 265 p 16.

323   18.   Telfer MW, Hesse PP, Perez-Fernandez M, Bailey RM, Bajkan S, Lancaster N. Morphodynamics,

324   boundary conditions and pattern evolution within a vegetated linear dunefield. Geomorphology. 2017; 290: 85-100

325   19.   Warren SG, Brandt RE, Hinton PO. Effect of surface roughness on bidirectional reflectance of Antarctic

326   snow. Journal of Geophysical Research-Planets. 1998;103(E11):25789-807.

327   20.   Greeley R., Iversen JD. Wind as a Geological Process: on Earth, Mars, Venus and Titan. 1985; Cambridge

328   University Press: Vol. 4. 67–106 .

329   21.   Toigo AD, French RG, Gierasch PJ, Guzewich SD, Zhu X, Richardson MI. General circulation models of

330   the dynamics of Pluto's volatile transport on the eve of the New Horizons encounter. Icarus. 2015;254:306-323.

331   22.   Kok JF. An improved parameterization of wind-blown sand flux on Mars that includes the effect of

332   hysteresis. Geophysical Research Letters. 2010;37.

333   23.   Kok JF. Difference in the Wind Speeds Required for Initiation versus Continuation of Sand Transport on

334   Mars: Implications for Dunes and Dust Storms. Physical Review Letters. 2010;104(7).

335   24.   Frezzotti M, Gandolfi S, Urbini S. Snow megadunes in Antarctica: Sedimentary structure and genesis.

336   Journal of Geophysical Research-Atmospheres. 2002;107(D18).

337   25.   Soderblom LA, Kirk RL, Lunine JI, Anderson JA, Baines KH, Barnes JW, et al. Correlations between

338   Cassini VIMS spectra and RADAR SAR images: Implications for Titan's surface composition and the character of

339   the Huygens probe landing site. Planetary and Space Science. 2007;55(13):2025-36.

340   26.   Hansen CJ, McEwen AS, Ingersoll AP, Terrile RJ. Surface and airborne evidence for plumes and winds on

341   Triton. Science. 1990;250(4979):421-4.

342   27.   Soderblom, LA, Kieffer SW, Becker TL, Brown RH, Cook AF, Hansen, CJ et al. Triton's geyser-like

343   plumes – discovery and basic characterization. Science. 1990; 250 (4979); 410-415

344   28.   Bertrand T, Forget F. Observed glacier and volatile distribution on Pluto from atmosphere-topography

345   processes. Nature. 2016; 540:86-89.

346   29.   Schmitt B, Philippe S, Grundy WM, Reuter DC, Côte R, Quirico E et al. Physical state and distribution of

347   materials at the surface of Pluto from New Horizons LEISA imaging spectrometer. 2017. Icarus; 289:229-260.

348   30.   Howard AD, Moore JM, Umurhan OM, White OL, Anderson RS, McKinnon WB, et al. Present and past

349   glaciation on Pluto. Icarus. 2017; 287:287-300.

350   31.   Eluszkiewicz J. On the microphysical state of the surface of Triton. Journal of Geophysical Research-

351   Planets. 1991;96:19217-29.

352   32.   Eluszkiewicz J, Stevenson DJ. Rheology of solid methane and nitrogen - applications to Triton.

353   Geophysical Research Letters. 1990;17(10):1753-6.

354   33.   Zent AP, McKay CP, Pollack JB, Cruikshank DP. Grain metamorphism in polar nitrogen ice on Triton.

355   Geophysical Research Letters. 1989;16(8):965-8.

356   34.   Pähtz T, Kok JF, Parteli EJR, Herrmann HJ. Flux Saturation Length of Sediment Transport. Physical

357   Review Letters. 2013;111(21): 218002.

358   35.   Fourriere A, Claudin P, Andreotti B. Bedforms in a turbulent stream: formation of ripples by primary linear

359   instability and of dunes by nonlinear pattern coarsening. Journal of Fluid Mechanics. 2010;649:287-328.

360   36.   Kaufmann E, Kömle NI, Kargl, G. Laboratory simulation experiments on the solid-state greenhouse effect

361   in planetary ices. Icarus, 2006;185:274-286

362   37.   Thomas N, Hansen CJ, Portyankina G, Russell PS. HiRISE observations of gas sublimation-driven activity

363   in Mars' southern polar regions: II. Surficial deposits and their origins. Icarus. 2010;205(1):296-310.

364   38.   Thomas N, Davidsson B, El-Maarry MR, Fornasier S, Giacomini L, Gracia-Berna AG, et al. Redistribution

365   of particles across the nucleus of comet 67P/Churyumov-Gerasimenko. Astronomy & Astrophysics. 2015;583:18.

366   39.   Jia P, Andreotti B, Claudin P. Giant ripples on comet 67P/Churyumov–Gerasimenko sculpted by sunset

367   thermal wind. Proceedings of the National Academy of Sciences. 2017; 114(10): 2509–2514.

368   40.   Fray N, Schmitt, B. Sublimation of ices of astrophysical interest: A bibliographic review.

369   Planetary and Space Science. 2009; 57: 2053-2080

370   41.   Cruikshank D, paper presented 49th Division of Planetary Sciences meeting, Provo, UT, 15 October 2017.

371   Abstract ID 102.06.

372   42.   Stern SA, Binzel RP, Earle AM, Singer KN, Young LA, Weaver HA, et al. Past epochs of significantly

373   higher pressure atmospheres on Pluto. Icarus. 2017; 287: 47-53.

374   43.   Filhol S., Sturm M. Snow bedforms: A review, new data, and a formation model. Journal of Geophysical

375   Research – Earth Surface. 2015;120(9):1645-1669.

376   44.   Cathles LM, Abbot DS, MacAyeal DR. Intra-surface radiative transfer limits the geographic extent of snow

377   penitents on horizontal snowfields. Journal of Glaciology. 2014;60(219):147-54.

378   45.   Moores JE, Smith CL, Toigo AD, Guzewich SD. Penitentes as the origin of the bladed terrain of Tartarus

379   Dorsa on Pluto. Nature. 2017;541(7636):188-90.

380   46.   Robbins SJ, Singer KN, Bray VJ, Schenk P, Lauer TR, Weaver HA et al. Craters of the Pluto-Charon

381   system. Icarus. 2017; 287: 187-206.

382   47.   NASA/John Hopkins University Applied Physics Laboratory/South West Research Institute. The rich

383   colour variations of Pluto. Available at http://photojournal.jpl.nasa.gov/catalog/PIA19952 (accessed 27/09/2016)

384   48.   NASA/John Hopkins University Applied Physics Laboratory/South West Research Institute. Pluto's Icy

385   Plains Captured in Highest-Resolution Views from New Horizons. Available at

386   http://photojournal.jpl.nasa.gov/catalog/PIA20336 (accessed 27/09/2016)

387   49.   NASA/John Hopkins University Applied Physics Laboratory/South West Research Institute. Pluto's Close-

388   up, Now in Color. Available at: http://photojournal.jpl.nasa.gov/catalog/PIA20213 (accessed 27/09/2016)

389   50.   NASA/John Hopkins University Applied Physics Laboratory/South West Research Institute. Ice Mountains

390   and Plains. Available at: http://photojournal.jpl.nasa.gov/catalog/PIA19954 (accessed 27/09/2016)

391   51.   Sides SC, Becker TL, Becker KJ, Edmundson KL, Backer JW, Wilson TJ, et al., paper presented 48th

392   Lunar and Planetary Science Conference, held 20-24 March 2017, at The Woodlands, Texas. LPI Contribution No.

393   1964, id.2739

394   52.   USGS Isis: Technical documents. Available at https://isis.astrogeology.usgs.gov/TechnicalInfo/index.html

395   (accessed: 27/03/2018).

396   53.   Peterson J. New Horizons SOC to Instrument Pipeline ICD. 2007. Available at https://pds-

397   smallbodies.astro.umd.edu/holdings/nh-j-lorri-3-jupiter-v1.0/document/soc_inst_icd/ (accessed: 27/3/2018)

398   54.   Kroy K, Sauermann G, Herrmann HJ. Minimal model for aeolian sand dunes. Physical Review E.

399   2002;66:031302.

400   55.   Kok JF, Parteli EJR, Michaels TI, Karam DB. The physics of wind-blown sand and dust. Reports on

401   Progress in Physics. 2012;75(10).

402   56.   Shao YP, Lu H. A simple expression for wind erosion threshold friction velocity. Journal of Geophysical

403   Research. 2000;105:22437-43.

404   57.   Iversen JD, White BR. Saltation threshold on Earth, Mars and Venus. Sedimentology. 1982;29:111–9.

405   58.   Almeida MP, Parteli EJR, Andrade Jr. JS, Herrmann HJ. Giant saltation on Mars. 2008;105:6222-6.

406   Proceedings of the National Academy of Science of the USA. 2008;105:6222-6.

407   59.   Pähtz T, Kok JF, Herrmann HJ. The apparent surface roughness of a sand surface blown by wind from an

408   analytical model of saltation. New Journal of Physics. 2012;14:043035.

409   60.   Sutton JL, Leovy CB, Tillman JE. Diurnal variations of the Martian surface layer meteorological

410   parameters during the first 45 sols at two Viking lander sites. Journal of Atmospheric Sciences. 1978;35:2346-2355.

411   61.   Sullivan R, Greeley R, Kraft M, Wilson G, Golombek M, Herkenhoff K, et al. Results of the Imager for

412   Mars Pathfinder windsock experiment. Journal of Geophysical Research. 2000;105:24547–62.

413   62.   Elbelrhiti H, Claudin P, Andreotti B. Field evidence for surface-wave-induced instability of sand dunes.

414   Nature. 2005;437:720-3.

415   63.   Pye K, Tsoar H. Aeolian sand and sand dunes. London: Unwin Hyman; 1990. 396 p.

416   64.   Matson DL, Brown RH. Solid-state greenhouse and their implications for icy satellites. Icarus. 1989:

417   77(1);67-81.

418   65.   Piqueux S, Christensen PR. North and south subice gas flow and venting of the seasonal caps of Mars: A

419   major geomorphological agent. Journal of Geophysical Reseach – Planets. 2008:113;E06005.

420   66.   Kaufmann E, Hagermann A. Experimental investigation of insolation-driven dust ejection from Mars' CO_2

421   ice caps. Icarus; 282:118-126

422   67.   Hapke B. Theory of reflectance and emittance spectroscopy, Cambridge University Press, New York. 1993.

423   68.   Grundy WM, Schmitt B, and Quirico E. The temperature-dependent spectrum of methane ice I between 0.7

424   and 5 micron sand opportunities for near-infrared remote thermometry. Icarus. 2002;155:486-496.

425   69.   Bertrand T, Forget F, Umurhan OM, Grundy WM, Schmitt B, Protopapa S et al. The nitrogen cycles on

426   Pluto over seasonal and astronomical timescales. Icarus. 2018; 309:277-296.

433 **Author contributions:**

434 MWT conducted the spatial analysis and image interpretation, coordinated the research and co-wrote the paper.

435 EJRP developed and conducted the numerical modelling and co-wrote the paper. JR coordinated the research and

436 co-wrote the paper. RAB produced and provided LORRI mosaicking. TB and FF provided data on

437 surface/atmosphere exchanges. FN performed calculations on the effectiveness of sublimation modelling. WMG

438 conducted the Hapke modelling. JMM, SAS and JS contributed to the manuscript. TRL produced and provided

439 LORRI mosaicking. RPB and AME provided circulation model data. HAW, CBO, LAY and KE are project

440 scientists and contributed to the mansucript. KR provided discussion of ideas.

441 **Competing interests:**

442 There are no competing interests to declare.

443 **Data and materials availability:**

444 The LORRI data are archived in the Planetary Data System (PDS) Small Bodies Node at https://pds-

445 smallbodies.astro.umd.edu/holdings/nh-p-lorri-3-pluto-v2.0/. MVIC data are available via the PDS at https://pds-

446 smallbodies.astro.umd.edu/holdings/nh-p-mvic-3-pluto-v2.0/

447

448

449 **Supplementary Materials**

450 www.sciencemag.org

451 The New Horizons Geology, Geophysics and Imaging Science Theme Team

452 Materials and Methods

453 Figs. S1, S2, S3, S4, S5

454 References (51-69)

Fig. 1. New Horizons fly-by imagery of landforms attributed to eolian origins. All images are unrectified and thus all scales are approximate. Color-composite MVIC images are shown here for context; dune identification was performed on greyscale LORRI images (shown below). A) Overview of Pluto centered on ~25° latitude, ~165° longitude, showing the locations of images B) and E) and figures 3A and S3 (47). B) The spatial context for SP and the AIM mountains to the west (48). Insets C) and D) show details of the highly regular spatial patterning which we attribute to eolian dune formation, and two newly-identified wind streaks (arrows x), along the margins of the SP/AIM border. Here the dunes show characteristic bifurcations (arrows y) and a superposition with SP's polygonal patterning (arrow z), suggesting a youthful age for these features (49). E) Two further wind streaks on the surface (x'), downwind of the Coleta de Dados Colles (4). These wind streaks, farther from the SP/AIM margin, are oriented differently to those close to the icefield's edge, and are still roughly orthogonal to the dunes there.

Fig. 2: Identified dunes (black lines) at the margins of western Sputnik Planitia (A). Prominent wind streaks are marked with orange lines. (B) Radial plot of the orientation of the dunes (n=331), and the direction orthogonal to the wind implied by the wind streaks close to the SP/AIM margin (orange dashed line; n=4; arithmetic mean, $\bar{x}$=203°). Because the dunes have a distinct shift in orientation (Fig. S1), the distribution of dunes in the three patches closest to the wind streaks within the dunefield (outlined in dashed green on A) has been separately highlighted on the radial plot, in green. These have a mean orientation of 204° (n=77), highlighted by the dashed green line. The dark blue line indicates the mean trend of the border of SP and the Al-Idrisi Montes in this area (194°). C) Frequency of dune spacings in clusters close to (red line representing dunes within the red dashed line of A) and far from (green line representing dunes within the green dashed line of A) the icefield/mountain interface. Dunes
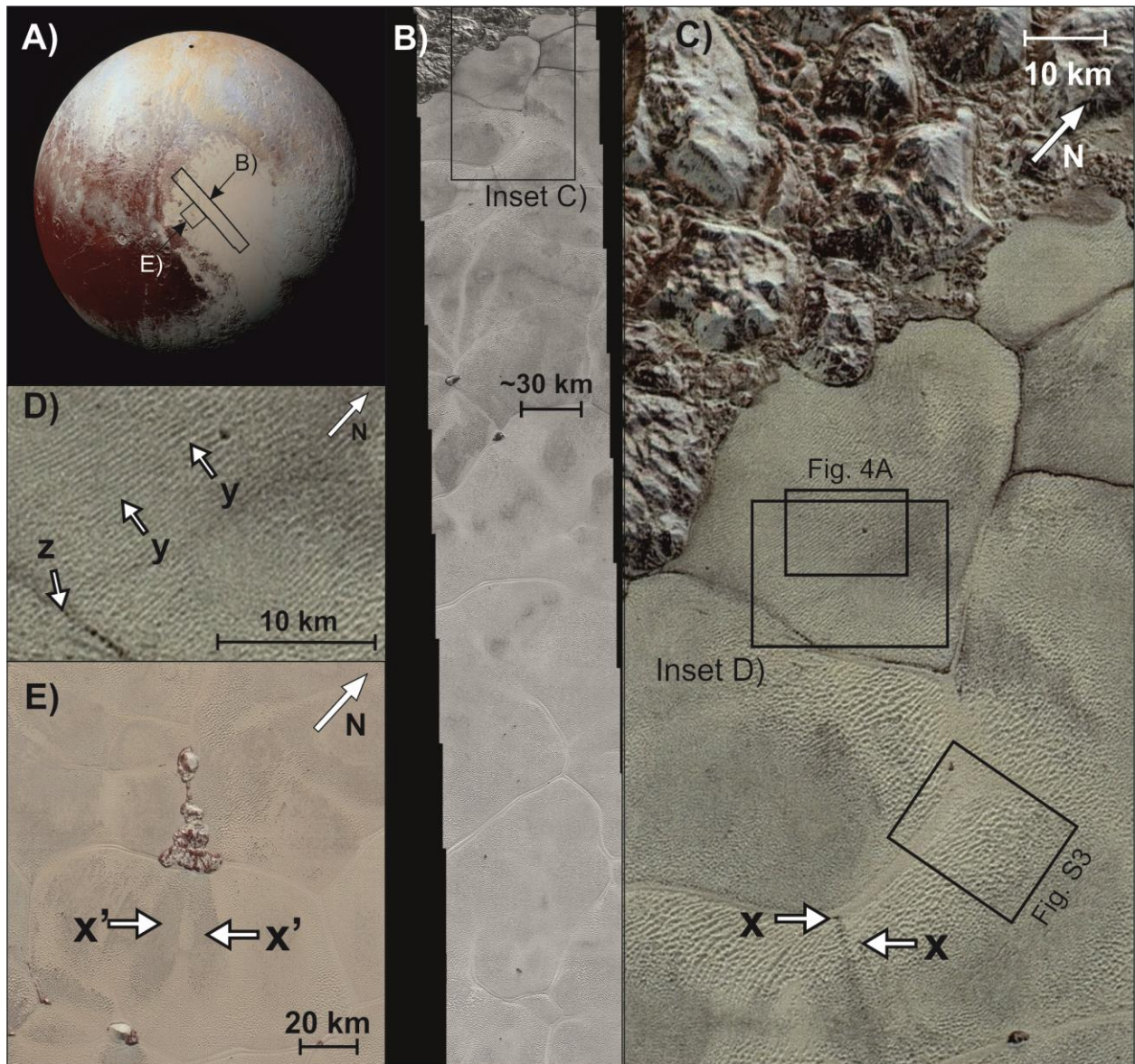
478 *farther from the mountains are significantly more widely-spaced ($\bar{x}$ = 700 m) than those close to*

479 *the mountains ($\bar{x}$ = 560 m).D) Detail of the image interpretation process of the highest*

480 *resolution swath, showing linear ridges, which sometimes bifurcate but are otherwise*

481 *remarkable for their regularity; E) The same image with ridge lines highlighted*

482 *Fig. 3: The western margin of Sputnik Planitia. A) shows transverse dunes in black, the margin*

483 *of the icefield and neighboring Al-Idrisi Montes to the northwest in blue, wind streaks close to*

484 *this margin in orange, and further wind streaks further from the mountains in yellow. There is an*

485 *orientation shift between the two sets of wind streaks, matching the correlation between the*

486 *distance to the margin of the icefield and mountains, and the orientation of the transverse dunes*

487 *(shown in inset B; wind streaks in orange). We interpret this as topography and/or surface*

488 *composition influencing regional wind regimes.*

489 *Fig. 4: Analogues and comparison with sublimation features. A) details of the dunes on western*

490 *Sputnik Planitia, centered on 34.35° 159.84° (location shown in Fig. 1). B) analogous terrestrial*

491 *transverse dunes of the Taklamakan Desert, western China (image © CNRS/SPOT, ©*

492 *DigitalGlobe and courtesy of Google Earth^{TM}), and C) the same location down-sampled to a*

493 *similar relative resolution as the Pluto dunes (i.e. approximately 5-10 pixels per crest-crest*

494 *spacing). D) the aligned and distorted sublimation features abundant on southern and eastern*

495 *SP (image centered on -4.78° 189.48°) and E) weakly-aligned to randomly oriented, shallow*

496 *sublimation pits.. F) an example of a landscape revealing both eolian and sublimation-derived*

497 *landforms at Mars' southern polar ice-cap from the Mars Reconnaissance Orbiter reveals both*

498 *dark eolian bedforms (dunes and ripples), as well as sublimation pits developing in the*

499 *underlying CO_2 ice (Image credit: NASA/JPL/University of Arizona, ESP_014342_0930_RED).*
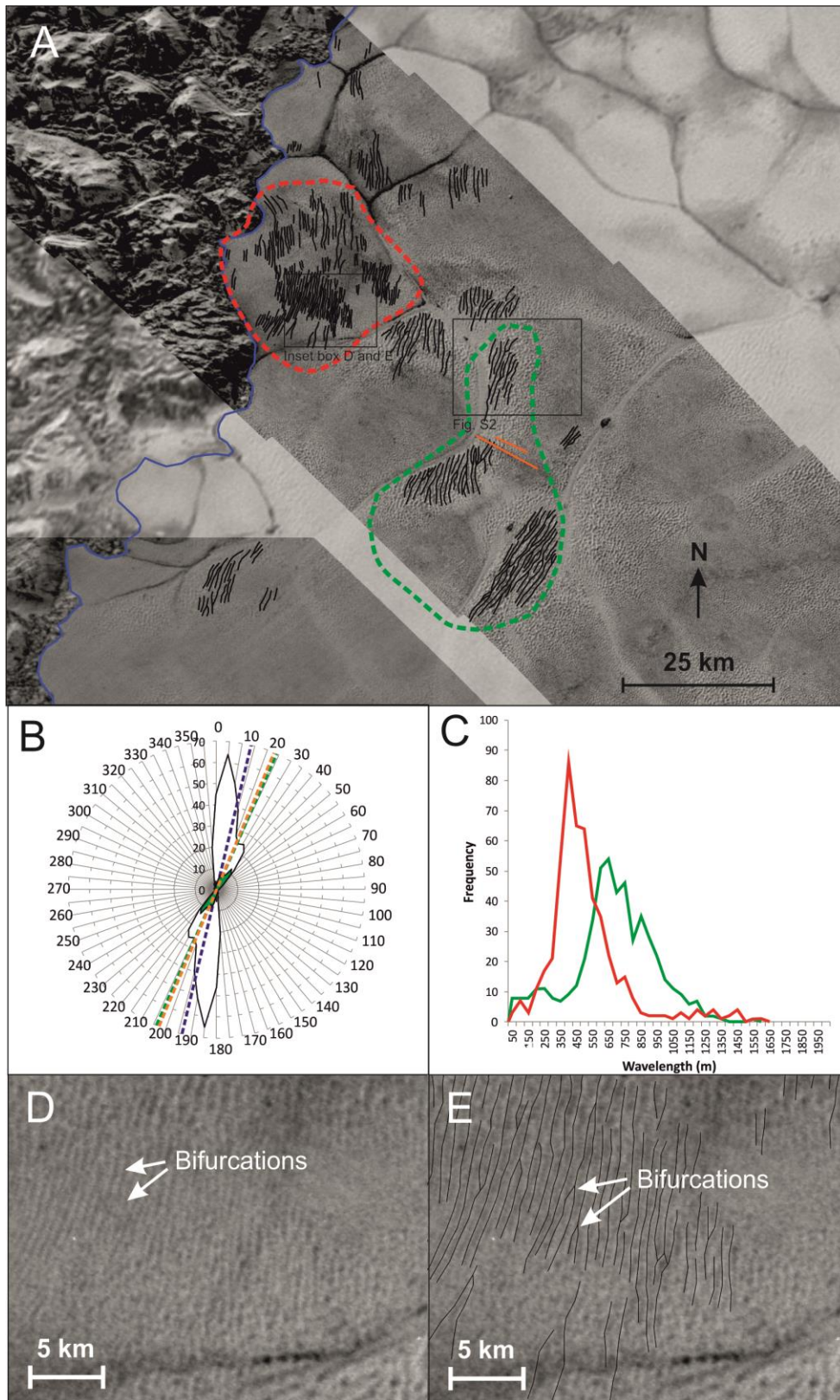
500   *Fig. 5. Minimal threshold wind speed for initiation (U_{ft}, orange line) and continuation (U_t, black*

501   *line) of saltation on Pluto, at a reference height of 10 m above the soil, computed for different*

502   *values of the average particle diameter (15). The dashed horizontal line indicates maximum*

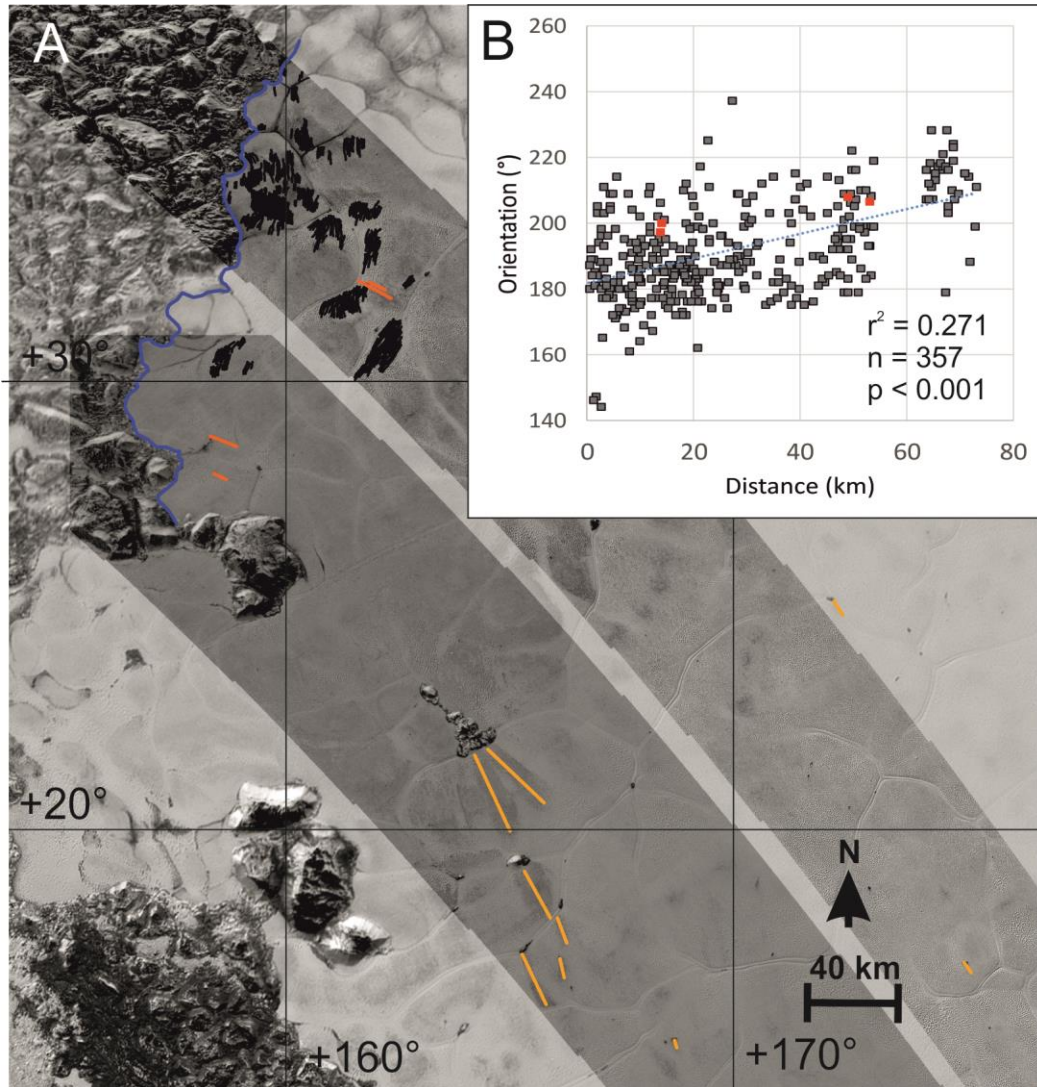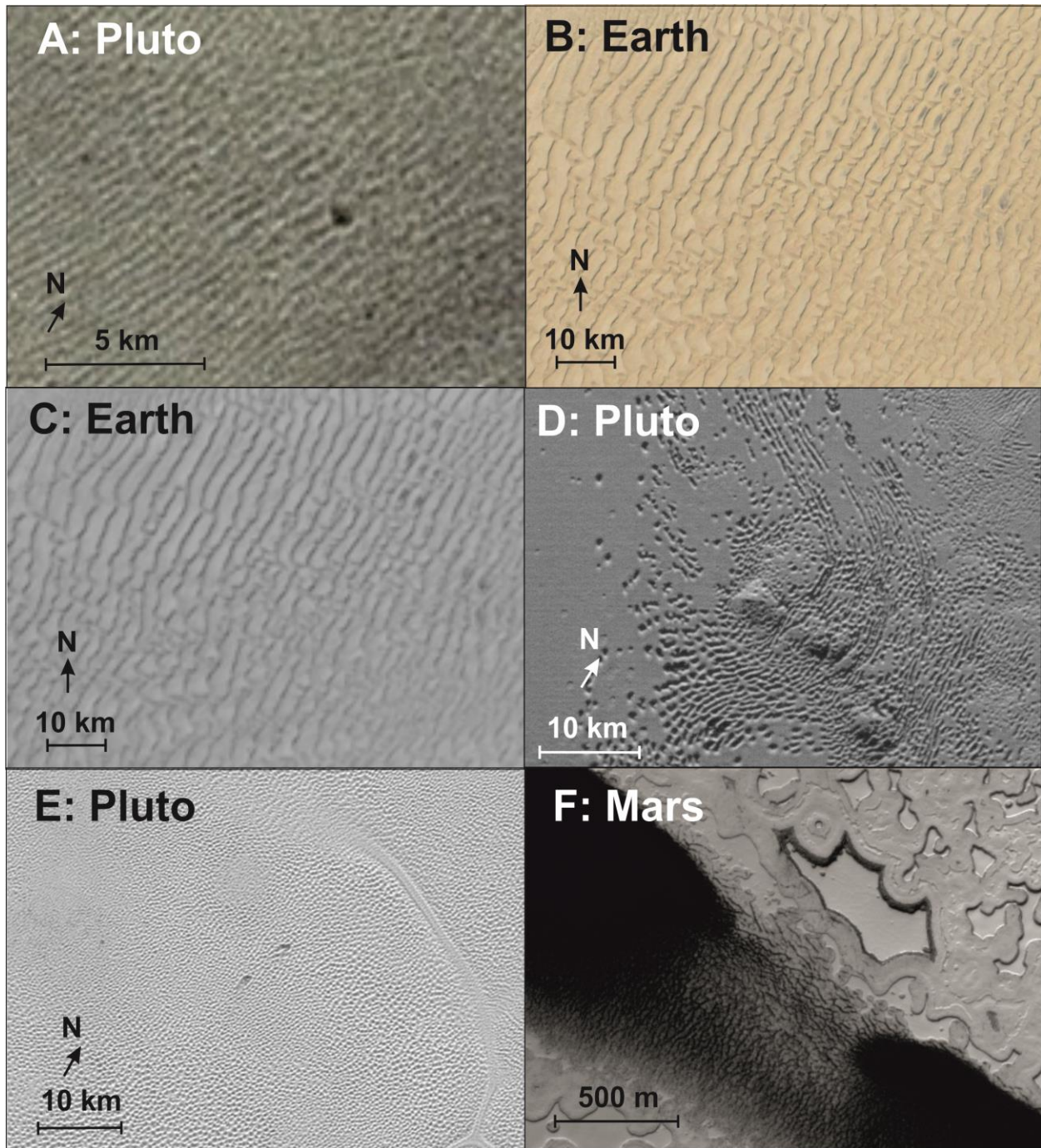503   *likely windspeeds at Pluto's surface.*
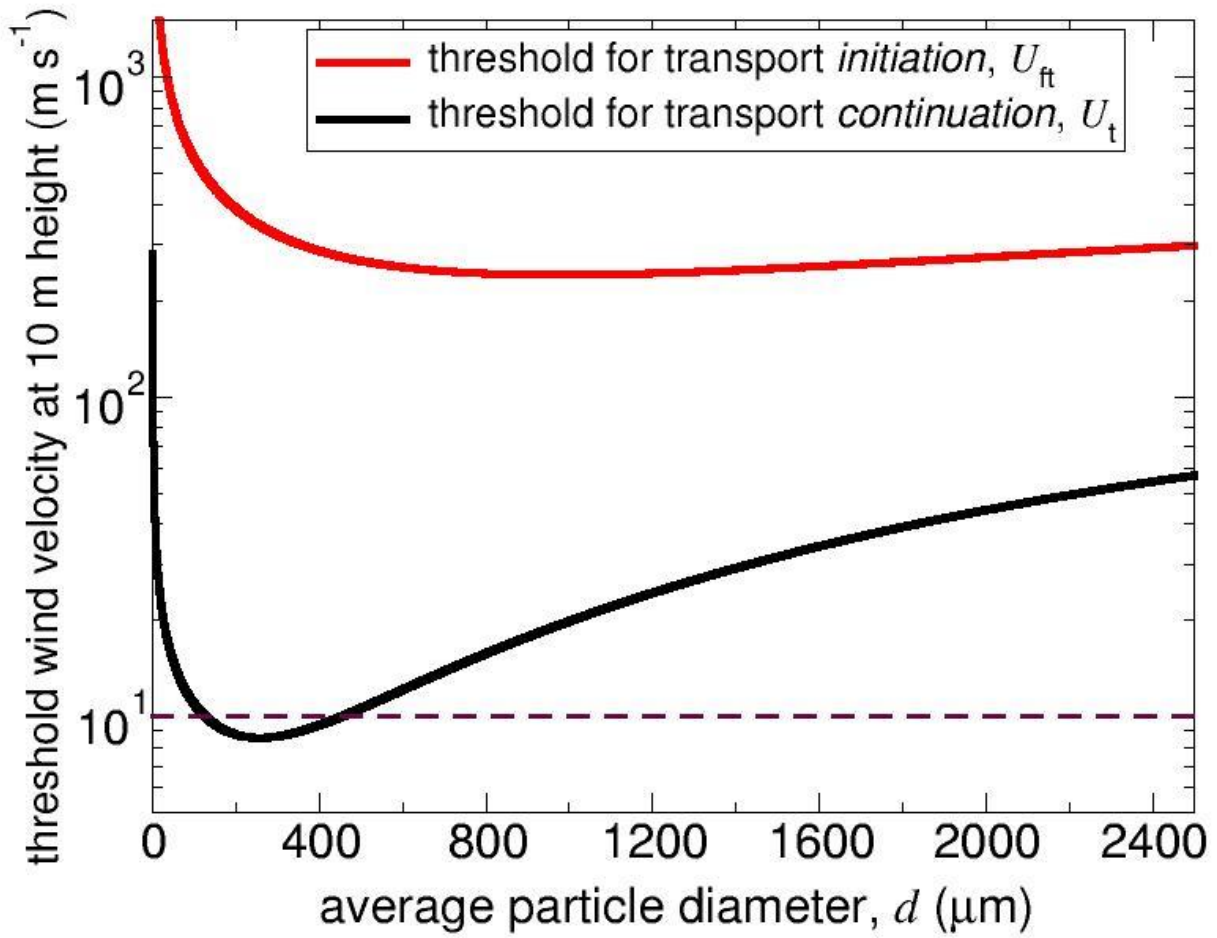
504

505
506   *Fig. 1*

507

508

Fig. 2

510

511   Fig. 3

A: Pluto
N
5 km

B: Earth
N
10 km

C: Earth
N
10 km

D: Pluto
N
10 km

E: Pluto
N
10 km

F: Mars
500 m

Fig. 4

515

Fig. 5

517

518
519
520
521
522

Supplementary Materials for

523
524

Dunes on Pluto

525

526 Matt W. Telfer, Eric J.R. Parteli, Jani Radebaugh, Ross A. Beyer, Tanguy Bertrand, François Forget, Francis
527 Nimmo, Will M. Grundy, Jeffrey M. Moore, S. Alan Stern, John Spencer, Tod R. Lauer, Alissa M. Earle, Richard P.
528 Binzel, Hal A. Weaver, Cathy B. Olkin, Leslie A. Young, Kimberley Ennico, Kirby Runyon, and the New Horizons
529 Geology, Geophysics and Imaging Science Theme Team.

530
531 Correspondence to: matt.telfer@plymouth.ac.uk

532
533
534 **This PDF file includes:**

535
536 The New Horizons Geology, Geophysics and Imaging Science Theme Team Materials and Methods
537 Figs. S1 to S5
538
539
540
541
542

543   **The New Horizons Geology, Geophysics and Imaging Science Theme Team**

544   Jeffrey M. Moore, NASA Ames Research Center, Moffett Field, CA 94035.

545   Richard P. Binzel, Department of Earth, Atmosphere, and Planetary Science, Massachusetts

546   Institute of Technology, Cambridge, MA 02139.

547   Marc W. Buie, Southwest Research Institute, Boulder, CO, USA.

548   Bonnie J. Buratti, Jet Propulsion Laboratory, California Inst. of Technology, Pasadena, CA.

549   Andrew F. Cheng, JHU/APL, Laurel, MD.

550   Kimberly Ennico, NASA Ames Research Center, Moffett Field, CA 94035.

551   W.M. Grundy, Lowell Observatory, Flagstaff, AZ.

552   J.J. Kavelaars, National Research Council of Canada, Victoria BC & Department of Physics and

553   Astronomy, University of Victoria, Victoria, BC, Canada.

554   Ivan R. Linscott, Stanford University, Stanford, CA.

555   William B. McKinnon, Washington University in St. Louis, St. Louis, MO.

556   Catherine B. Olkin, JHU/APL, Laurel, MD

557   Harold J. Reitsema, Ball Aerospace (retired), Boulder, CO.

558   Dennis Reuter, NASA's Goddard Space Flight Center, Greenbelt, MD 20771.

559   Paul Schenk, LPI, Houston, TX.

560   Mark Showalter, SETI Institute, Mountain View, CA.

561   John Spencer   John R. Spencer, SwRI, Boulder, CO.

562   S. A. Stern, Southwest Research Institute, Boulder, CO, USA.

563   G. Leonard Tyler, Stanford (Emeritus), Stanford, CA.

564   H. A. Weaver, Johns Hopkins University Applied Physics Laboratory, Laurel, MD, USA.

565   Leslie A. Young, Southwest Research Institute, Boulder, CO, USA.

566

567   **Materials and Methods**

568   <u>S 1 Image Interpretation</u>

569   The names Sputnik Planitia and Al-Idrisi Montes are formally approved by the International

570   Astronomical Union (IAU); all other names referred to within the text are informal.

571   Landforms were interpreted from the P_MVIC_LORRI_CA (75 m per pixel) and

572   P_MPAN_LORRI (124 m per pixel) observations georeferenced to a global mosaic within ESRI

573   ArcGIS 10.3, projected to a spheroid of radius 1188.3 km. The LORRI instrument is a

574   panchromatic sensor in the range 350 to 850 nm with an unfiltered 1024×1024 pixel Charged-

575   Couple Device (CCD). The field of view is 0.29° (*8*). A global LORRI image mosaic was used

576   for contextualizing the area of interest. Images with variable resolutions (e.g. Fig. 1) are

577   comprised of lower-resolution mosaics taken from more distant observations from the LORRI

578   instrument, with superimposed swathes of higher spatial resolution images from the closest

579   observations. For all LORRI image mosaics, the individual, PDS (Planetary Data System:

580   https://pds.nasa.gov/) EDR (Experiment Data Record) images were processed using the

581   Integrated Software for Imagers and Spectrometers (ISIS 3) (*51,52*). Images were converted

582   from raw Data Numbers to *I/F* (the ratio of reflected to incident flux) units via radiometric

583   equations (*53*). These images were then processed with the ISIS program *photomet* in order to

584   correct for the range of illumination and viewing geometries, map-projected with the ISIS

585   *cam2map* program, and finally mosaicked together with the ISIS *noseam* program.

586   Features were manually identified and digitized, based on an ontology limited to features with

587   high length/width ratios (i.e. clear alignment) and a length of >1 km. Dune spacing was obtained

588   by assigning 500 random points along the crest lines within dune 'clusters' using ArcGIS 10.3,

589   and using ArcGIS's Near function to find the distance to the nearest adjacent feature. Samples

590   near the end of isolated dunes thus might indicate a spuriously high spacing, which probably

591   accounts for the high outliers in Fig. 2.

592   MVIC consists of seven CCD arrays. Two are panchromatic, and four provide color or near

593   infrared detection capabilities (BLUE (400 to 550 nm filters), RED (540 to 700 nm), NIR (780 to

594   975 nm), and a narrow methane-sensitive band, based around the 890 nm absorption line

595   ("CH4," 860 to 910 nm). Fig. S4 is based on the highest resolution MVIC scan

596   ("P_COLOR_2"), with the unique MET ID 0299178092, archived in the PDS. Mid- observation

597   time was 2015-07-14 11:10:52 Coordinated Universal Time, corresponding to a range from

598   Pluto's center of 33963 km, sub-spacecraft longitude and latitude of 168.03 E, 25.98 N, and a

599   phase angle of 38.80°.

600

601   S2 Modeling

602

603   This Section presents the equations used to obtain the minimal threshold wind velocities required for initiation and

604   continuation of sediment transport, U_{ft} and U_t, respectively (Fig. 5). Moreover, a description of the method

605   developed for obtaining the average grain size d and surface wind speed U in the transverse dune field of Sputnik

606   Planitia (Fig. S5) is provided.

607

608   In subsection **S2.1**, the equations for obtaining U_{ft} and U_t are shown, while in the three subsequent subsections, the

609   method for obtaining d and U from the crest-to-crest distance of the transverse dunes is presented. As discussed in

610   the main text, this distance scales with the saturation length of sediment transport, L_{sat}, that is, the transient length

611   needed by the mass flux of particles in the transport layer to adapt to a change in flow conditions (*34*). An analytical

612   model for reliably computing L_{sat} as a function of the attributes of sediment and atmosphere in rarified atmospheres

613   has been derived (*34*). In Subsection **S2.2**, we list the main equations of this model, which we use to compute L_{sat} in

614   Sputnik Planitia as a function of grain size and wind speed. Moreover, an analytical model to obtain L_{sat} from the

615   crest-to-crest distance of the "elementary" transverse dunes – which are the smallest transverse dunes formed by the

616   wind on a flat sand surface – has been derived (*54*). In Subsection **S2.3** we list the equations of this model while in

617   Subsection **S2.4** we present our method to constrain d and U in Sputnik Planitia by combining models (*34*) and (*35*).

618

619   Subsection **S2.5** considers these results in the light of the forces needed to loft a particle under surface and

620   atmospheric conditions of SP. The final subsection, **S2.6**, justifies the assertion that the absorption of the MVIC CH_4

621   filter is consistent with the grain sizes proposed by the modelling of sections **S2.1 – S2.4** are supported.

622

623   S2.1 Threshold wind velocities for initiation and continuation of saltation on Pluto

624

625   *S2.1.1 Minimal threshold wind shear velocity for transport initiation, u_{ft}*

626

627   Sediment transport begins when the wind shear velocity u, which is proportional to the mean flow velocity gradient

628   in turbulent boundary layer flow, overcomes a minimal threshold value u_{ft}. A mathematical model for u_{ft} is

629   obtained by balancing the entraining forces (aerodynamic lift and drag) against the stabilizing forces (attractive

630   inter-particle forces and gravity), which leads to the following equation,

631

632
$$u_{ft} \approx A_N \sqrt{\frac{\rho_p - \rho_a}{\rho_a} gd + \frac{\zeta}{\rho_a d}} \quad \text{(S1)}$$

633

634   where ρ_p and ρ_a denote the densities of particles and air, respectively, g is gravity, d is the average diameter of the

635   particles, $A_N \approx 0.1$ and $\zeta \approx 5 \times 10^{-4}$ N/m is an empirically determined parameter that scales with the strength of

636   the attractive forces between the particles (54, 55). The first term in the square-root of Eq. S1 accounts for the

637   balance between gravity and aerodynamic forces, while the second term incorporates the effect of attractive inter-

638   particle forces (mainly van der Waals forces), which become significant when particle sizes decrease down to values

639   below 60 μm. A different mathematical formulation for u_{ft}, which leads to results not much different from the ones

640   from Eq. S1, has been obtained (56). In this model, A_N is determined by empirical expressions that encode the effect

641   of inter-particle cohesion; that is A_N depends on d, while $\zeta = 0$ (56).

642

643   *S2.1.2 Minimal threshold wind shear velocity for saltation continuation, u_t*

644

645   Once initiated, eolian transport of the sediment particles along the surface can take place through several modes, in

646   particular creep, that is, particles sliding or rolling along the surface, and saltation, which consists of particles

647   moving through nearly ballistic loops, thereby ejecting new particles upon collision with the ground (splash).

648   Moreover, once initiated, particle transport along the surface can be sustained at lower wind speeds because

649   entrainment of new particles into flow occurs mainly as a consequence of grain-bed collisions. Under terrestrial

650   conditions, the threshold for saltation continuation (or impact threshold) u_t is about 80% the threshold for saltation

651   initiation, u_{ft} (15). However, recent theory and numerical simulations showed that the ratio u_t/u_{ft} depends on

652   atmospheric conditions. Specifically, this ratio may decrease substantially under conditions of lower atmospheric

653   density and gravity, since such conditions lead to higher saltation trajectories, larger particle velocities and more

654   intense splash (57, 58). This stronger hysteresis of the threshold wind speed for saltation in lower atmospheric

655   density has been explicitly taken into account in theoretical work (59), which led to the following equation for u_t,

656

657 $$u_t = \kappa(V_{rs} + V_0) \cdot [(1 - \eta) \cdot \ln(z_{mt}/z_0)]^{-1}, \quad (S2)$$

658

659 where $\kappa = 0.4$ is the von Kármán constant; V_{rs} is the steady-state value of the difference between particle and fluid

660 velocities (58); V_0 is the average particle slip velocity – defined as the mean of the average horizontal (downwind)

661 components of the particle velocities at ejection and impact, respectively; the constant $\eta = 0.9$ describes how

662 efficiently the wind accelerates the grains within the transport layer at the threshold for sediment

663 transport; z_{mt} denotes an effective height of the average grain motion, and z_0 is the surface roughness of the

664 quiescent bed.

665

666 The values of V_{rs}, V_0 and z_{mt} are obtained from the following expressions (58),

667

668 $$V_{rs} = \sqrt{8\mu(s - 1)gd/9 + (8v/d)^2} - 8v/d, \quad (S3)$$

669

670 $$V_0 = 16.2\sqrt{gd + 6\zeta/[\pi\rho_p d]}, \quad (S4)$$

671

672 $$z_{mt} = \beta\gamma\sqrt{V_{rs}V_t^3} \cdot [\mu g]^{-1}, \quad (S5)$$

673

674 where $s = (\rho_p - \rho_a)/\rho_a$, v is the kinematic viscosity and μ stands for the Coulomb coefficient associated with the

675 effective frictional force that the soil applies on the transport layer per unit soil area in the steady-state (34). For

676 transport in the eolian regime, $\mu = 1$ (34). Furthermore, $\beta \approx 0.095$ is the ratio between the average work rate per

677 unit soil area in the vertical motion and that in the horizontal motion and $\gamma = z_{mt}/z_s \approx 0.17$, with z_s standing for

678 the characteristic height of the exponential decay of the grain-borne shear stress, while V_t, the average grain velocity

679 at threshold, is given by the equation,

680

681 $$V_t = V_0 + \eta V_{rs}/[1 - \eta]. \quad (S6)$$

682

683   Moreover, the surface roughness z_0 is given by the equation (55),

684

685    $$z_0 = d \exp(-\kappa B), \quad \text{(S7)}$$

686

687   where

688

689    $$B = 8.5 + \left[2.5 \ln(R_p) - 3 \right] \cdot \exp\left\{ -0.11 \left[\ln(R_p) \right]^{2.5} \right\}, \quad \text{(S8)}$$

690

691   with $R_p = u_t d / \nu$.

692

693

694   *S2.1.3 Minimal threshold wind shear velocities under atmospheric conditions of Pluto*

695

696   We calculate the minimal threshold wind shear velocity u_{ft} as a function of the particle diameter using Eq. S1, with

697   Pluto's gravity $g = 0.658$ m/s^2, methane ice particles of density $\rho_p = 494$ kg/m^3 and an atmospheric density $\rho_p =$

698   9.1×10^{-5} kg/m^3, consistent with surface temperature of 37 K and pressure of 1 Pa atmosphere composed

699   predominantly of N$_2$ (5).

700

701   Moreover, the minimal threshold wind shear velocity u_t for sustained transport is computed as a function of average

702   grain diameter under the attributes of atmosphere specified in the previous paragraph (the associated kinematic

703   viscosity is $\nu = 0.02$ m^2/s).

704

705   From u_t and u_{ft}, the corresponding threshold wind speeds at the reference height of 10 m can be computed using the

706   equation

707

708    $$U = \frac{u}{\kappa} \ln \frac{z}{z_0}, \quad \text{(S9)}$$

709

710   where z is the height above the ground. By taking $z = 10$ m and z_0 computed with Eq. S7 as a function of the mean

711   particle size d, and by substituting the values of u_{ft} and u_t obtained with Eqs. S1 and S2, respectively, as functions

712   of d, we obtain the result shown in Fig. 5.

713

714   We see that grain sizes between 100 and 400 μm correspond to the lowest wind velocities required to sustain

715   sediment transport. The associated wind shear velocities are between 0.4 and 0.6 m/s. These wind shear velocities

716   are common to sand deserts of the Earth and fall within the range of average values of u measured on Martian soils

717   (60,61).

718

719   <u>S2.2 Flux saturation length of eolian sediment transport on Pluto</u>

720

721   The saturation length of the eolian sediment flux is computed using the equation (34)

722

723      $L_{sat} = 3c_v V_s V_{rs} F K \mu^{-1} g^{-1}$ (S10)

724

725   where $c_v \approx 1.3$ is the steady-state value of the particle speed square correlation, obtained from measurements of the

726   particle velocity distribution (34). The average particle velocity in the steady-state, V_s, is given by the equation

727

728      $V_s = V_t + [3u_t/2\kappa] \cdot \ln(V_s/V_t) + [u/\kappa] \cdot F_\gamma(u_t/u),$ (S11)

729

730   where

731

732      $F_\gamma(x) = (1 - x) \cdot \ln(1.78\gamma) + 0.5(1 - x^2) + E_1(\gamma) + 1.154(1 + x \ln x)(1 - x)^{2.56}$ (S12)

733

734   with $E_1(x)$ standing for the exponential integral function (34, 58). Moreover, the variables F and K are given by the

735   expressions

736

737 $$F = [V_{rs} + 16\,v/d] \cdot [2V_{rs} + 16\,v/d]^{-1}, \quad (S13)$$

738

739 $$K = \frac{1 + F^{-1}[(V_s + V_{rs})/(2V_{rs})][(u/u_t)^2 - 1]}{1 + [(V_s + V_{rs})/(2V_s)][(u/u_t)^2 - 1]}. \quad (S14)$$

740

741 By obtaining the saturation length from the dune size, it is possible to constrain possible values of u and d formative

742 of the transverse dunes. This procedure is explained in the next two subsections.

743

744 S2.3 Flux saturation length from the crest-to-crest distance of the elementary transverse dunes

745

746 The flux saturation length can be obtained from the wavelength (crest-to-crest-distance) of the smallest transverse

747 dunes that a wind forms on a flat sand sheet ("elementary transverse dunes") using an analytical model (35).

748 Examples of such elementary transverse dunes are superimposed bedforms emerging on a flat surface or on top of a

749 large barchan dune, for instance due to a storm wind that makes a small angle with the prevailing transport direction

750 (62). An important assumption we have to make to use this model is, thus, that the size of dunes observed in the

751 images (~ 700 m) is not substantially larger than the size of the elementary dunes produced by the action of wind on

752 a flat sand sheet on Pluto. That is, the dunes did not increase significantly in size due to amalgamation and merging

753 into much larger or giant bedforms; to compare, the size of elementary dunes on Earth and Mars is about 10 m and

754 100 m, respectively (55). This is a plausible assumption for the dune field of Sputnik Planitia given the very young

755 age of this field, as discussed in the main text. The spatial wind shear stress on top of a flat bed with small

756 perturbation $h(x)$ in the vertical direction can be computed (35). The Fourier-transformed shear stress $\hat{\tau}(k)$ can be

757 written as:

758

759 $$\hat{\tau} = \tau_0 (A + iB) k \hat{h}, \quad (S15)$$

760

761 where ^ denotes the Fourier-transformed value of the corresponding quantity, k is the wavenumber, and A and B can

762 be approximated by the expressions (34),

763

$$A(R) = 2 + \frac{1.072 + 0.093069R + 0.10838R^2 + 0.024835R^3}{1 + 0.041603R^2 + 0.0010625R^4}, \quad \text{(S16)}$$

764

765

$$B(R) = \frac{0.036989 + 0.15765R + 0.11518R^2 + 0.0020249R^3}{1 + 0.0028725R^2 + 0.00053483R^4}, \quad \text{(S17)}$$

766

767

768 with $R = \ln(2\pi/\kappa z_0^*)$. The wavelength $\lambda = 2\pi/k_{\max}$ of the dunes corresponds to the wavenumber $k_{\max}$ under

769 which the dunes grow fastest. By using instability analysis (35), it has been shown that λ is related to the saturation

770 length L_{sat} through the equation,

$$\frac{2\pi L_{\text{sat}}}{\lambda} = X^{-1/3} - X^{1/3}, \quad \text{(S18)}$$

771

772

773 where the quantity X is defined as,

774

$$X = -\frac{\tilde{B}}{\tilde{A}} + \sqrt{1 + \frac{\tilde{B}^2}{\tilde{A}^2}}, \quad \text{(S19)}$$

775

776

777 while $\tilde{A}$ and $\tilde{B}$ incorporate dependence on the flow shear velocity (u),

778

$$\tilde{A} = A(R_{\max}) - \frac{\gamma_c A(R_{\max})}{1 + \gamma_c} \cdot \frac{u_t^2}{u^2}, \quad \text{(S20)}$$

779

780

$$\tilde{B} = B(R_{\max}) - \frac{\gamma_c B(R_{\max}) + \mu_c^{-1}}{1 + \gamma_c} \cdot \frac{u_t^2}{u^2}. \quad \text{(S21)}$$

781

782

783 In the equations above, $R_{\max} = \ln[2\pi/(k_{\max}z_0^*)] = \ln[\lambda/z_0^*]$, $\mu_c \approx \tan(32°)$ is the dynamic angle of repose of the

784 sand, and $\gamma_c \approx 0$ for eolian transport.

785

786   The apparent roughness z_0^*, which is the surface roughness in the presence of the transport layer, is obtained from

787   the equation,

788

789
$$\ln\left(\frac{z_0^*}{z_0}\right) = \left(1 - \frac{u_t}{u}\right)\ln\left(\frac{z_s}{1.78z_0}\right) - 1.154\left[1 + \frac{u_t}{u}\ln\left(\frac{u_t}{u}\right)\right]\left(1 - \frac{u_t}{u}\right)^{2.56}, \qquad \text{(S22)}$$

790

791   with $z_s = z_{mt}/\gamma$.

792

793   <u>S2.4 Grain size and wind speed that formed the transverse dunes of Sputnik Planitia</u>

794

795   Our method to obtain the possible values of u and d (or, equivalently, U and d) that formed the transverse dunes in

796   Sputnik Planitia consists of numerically solving the following equation,

797

798    $L_{sat;d,u} = L_{sat;\lambda}$,   (S23)

799

800   where $L_{sat;d,u}$ denotes the right-hand side of Eq. S10 and $L_{sat;\lambda}$ is obtained from Eq. S18, that is, $L_{sat;\lambda} =$

801    $\left[X^{-1/3} - X^{\frac{1}{3}}\right] \cdot \lambda/(2\pi)$.

802

803   By solving Eq. S23, and using Eq. S9 to obtain the wind velocity at 10 m height, we obtain Fig. S5. This shows the

804   only values of d and U that lead to transverse dunes with spacing $\lambda = 560$ m and $\lambda = 700$ m, which are the values

805   observed at the transverse dune field of Sputnik Planitia (see main text). From Fig. S5 we see that the transverse

806   dunes consist of grain sizes that are, on average, not larger than ~370 μm (for the larger average crest-to-crest

807   distance of 700 m). Considering that the most probable wind speeds are within the region below this horizontal line

808   in Fig. S5, it can be seen from this figure that the characteristic grain size of the transverse dunes is not smaller than

809   ~210 μm. Furthermore, given the upper bound of 10 m/s, the grain size leading to the observed crest-to-crest

810   distances is most probably within the range $210 \lesssim d\,/\mu m \lesssim 310$ (see Fig. 3B). This range of grain sizes

811   corresponds to the following most probable range of wind velocity U at 10 m height (see Fig. 3B): $8.5 \lesssim$

812    $U/(\text{m/s}) \lesssim 10$.

813

814

815   These ranges of grain size and wind velocity are fully consistent with the average size of sediments composing Earth

816   dunes and wind speed formative of eolian bedforms in terrestrial dune fields (*17, 60*).

817

818   S2.5 The role of sublimation in initial particle lofting

819

820   Given the high shear velocities required for initial entrainment of particles under Pluto's surface conditions, here we

821   explore the feasibility of sublimation as a mechanism for particle lofting. The complexities of considering the

822   sublimation of the likely mixed-ice composition (probably CH_4 and N_2) of the surface of SP are substantial, and thus

823   here we consider the most conservative scenario for lofting particles; that the sediment comprising the dunes is the

824   denser N_2 ice.

825

826   Solid-state greenhouse effects have been shown to heat the subsurface (*64*), and the effects of this in generating

827   ejecta have been demonstrated theoretically (*65*) and experimentally (*66*) in thin atmospheres. If a subsurface cavity

828   is exposed to the surface by sublimation, the initial escape velocity will be the thermal velocity (~100 ms^{-1}).

829   Resultant drag imposed on particles, per unit area, is approximated by ρv^2 where ρ is the fluid density and v the fluid

830   velocity. Using the ideal gas law and considering the weight of the particle, we can thus state that:

831

832    $v = \frac{\sqrt{r \rho_s g R T}}{P \mu}$ (S24)

833

834   where r is the particle radius, ρ_s is the particle density, g is gravity, R the gas constant, T the gas temperature, P the

835   gas pressure and μ the molar mass of the gas. Using conservative Pluto surface conditions, and solving for P, the

836   pressure needed to support a particle 200 μm in radius is only 0.1 Pa at 50K. However, this should be regarded as an

837   indicative figure rather than a definitive answer, as a number of complications could change this value. These

838   include the likely overestimate of the effective velocity due to atmospheric interaction, and the complications likely

839   to result from rate of the sublimation of lofted particles. Conversely, the likely scenario of mixed-composition ices

840   may favor particle lofting; at the nitrogen frost point temperature, pure methane ice particles mixed with nitrogen

841   should not sublime at all. As they are slightly heated by the sun, they should sublimate the nitrogen ice that they

842   touch and be readily put aloft by the condensation flow, and thus provide an initial entrainment.

843

844   <u>S2.6 Modeling the size of particles responsible for the MVIC CH_4 filter observation</u>

845

846   New Horizons' Multi-Spectral Visible Imaging Camera (MVIC) has four interference filters, one of which passes

847   wavelengths from 860 to 910 nm, where CH_4 ice has a characteristic absorption band (*9*). Using this filter, along

848   with two others covering 540-700 nm and 780-975 nm, it is possible to estimate the equivalent width of absorption

849   in the CH_4 filter, which can be attributed to CH_4 ice. This CH_4 equivalent width has been mapped on the encounter

850   hemisphere (*6*). Examining the study area shows that many of the areas identified as having dunes or wind streaks

851   show greater CH_4 absorption than surrounding areas, as shown in Fig. S4, where the equivalent width map is

852   superposed in pink on New Horizons LORRI imagery of the region. The CH_4 equivalent width varies across the

853   scene from around 0.5 nm at lower right to as high as 3 nm corresponding to the centers of some of the convection

854   cells near Al-Idrisi Montes. Localized areas of much higher absorption can be seen within Al-Idrisi, and could

855   represent potential sources of CH_4 ice particles.

856

857   To check if 200 to 300 micron CH_4 ice particles could produce the observed absorption, we ran Hapke models (e.g.

858   *67*) to account for the multiple scattering effect in a granular medium. For this region, the incidence angle is about

859   41 degrees, emission angle is about 5 degrees, and phase angle is 39 degrees, so the observation was well outside of

860   any opposition surge, and thus we set B_0 to zero. We used Hapke's equivalent slab model to compute the single

861   scattering albedo as a function of wavelength, setting the real part of the refractive index to a constant 1.3 and the

862   imaginary part to 40 K values (*68*). We assumed an isotropic single scattering phase function. For 200 micron

863   particles, the model produced a spectrum in which the CH_4 equivalent width was 3.8 nm and for 300 micron

864   particles, we found an equivalent width of 4.7 nm. These values are somewhat higher than what was observed in the

865   MVIC images, but would be consistent with patchy coverage by CH_4 ice particles in that size range in the areas of

866   northwest SP where CH_4 absorption was strongest.

867
868
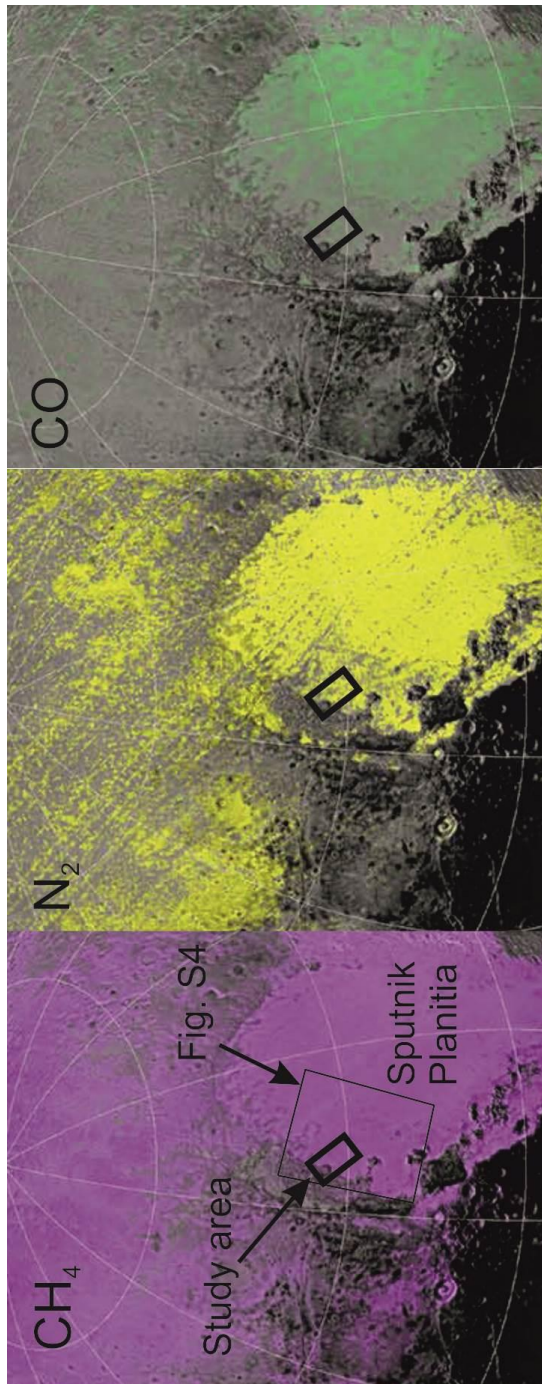
Fig. S1.
Position of the dunes (within the box) overlaid on the surface compositions (*6*) of A) methane, CH_4, B) nitrogen, N_2, and C) carbon monoxide, CO. The location of the dunefield at the western margin of Sputnik Planitia shows a surface composition dominated by N_2 and CH_4 ices. The location of Fig. S4 is also indicated here. Figure modified from (*6*).
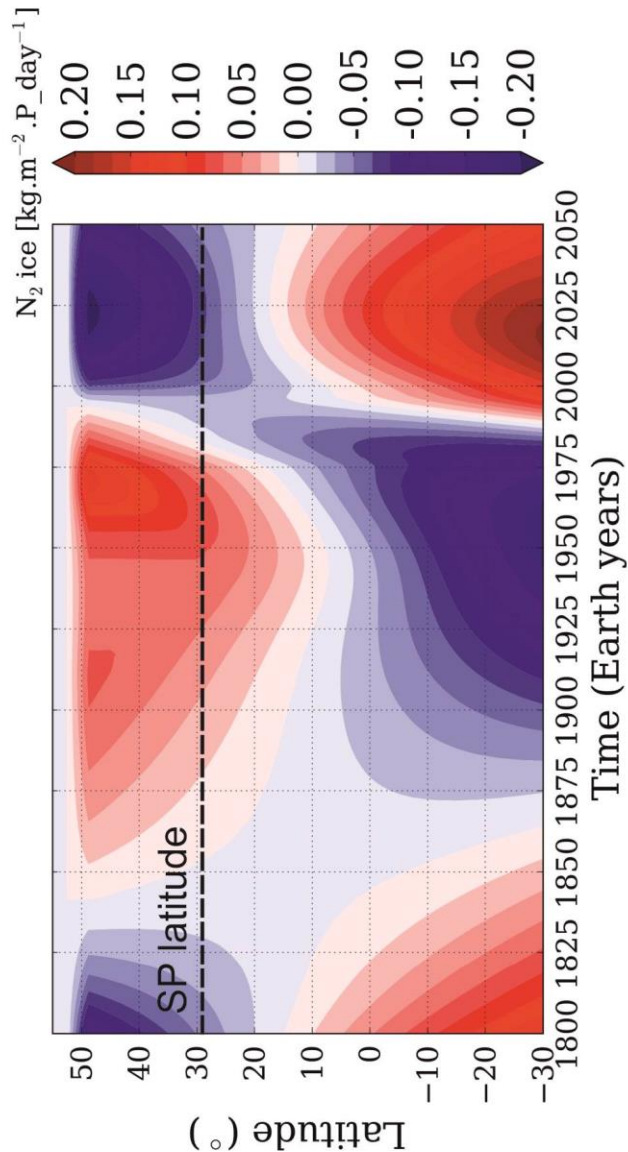
877

Fig. S2

878
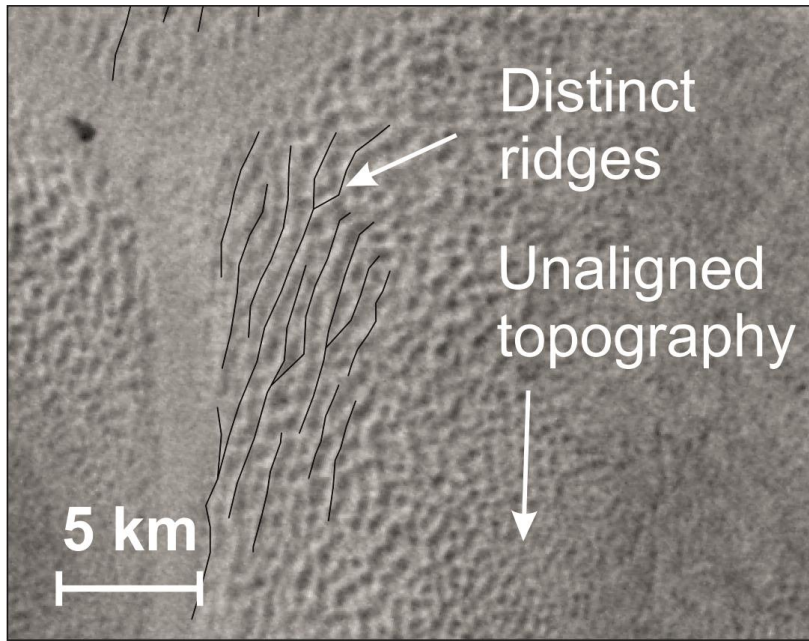
879 Fig. S2. The edge of the area of distinct linear features, where the surface changes to an
880 unaligned, scalloped relief. Location shown on Fig. 1.
881

Fig. S3

The accumulation and loss of N_2 ice over a timescale covering approximately one Pluto year (here from the terrestrial period 1800 to 2015), obtained with a volatile transport model within a post-encounter Pluto General Circulation Model (the model described in *16* and *69*). Note that at +35°, N_2 ice condensed in SP from 1820 to 1955 with a rate of few tens of micrometers per day (P_day refers to one Pluto day), whereas currently it is experiencing net sublimation. This is consistent with the observed degradation of eolian landforms following a period of enhanced sediment supply.

893
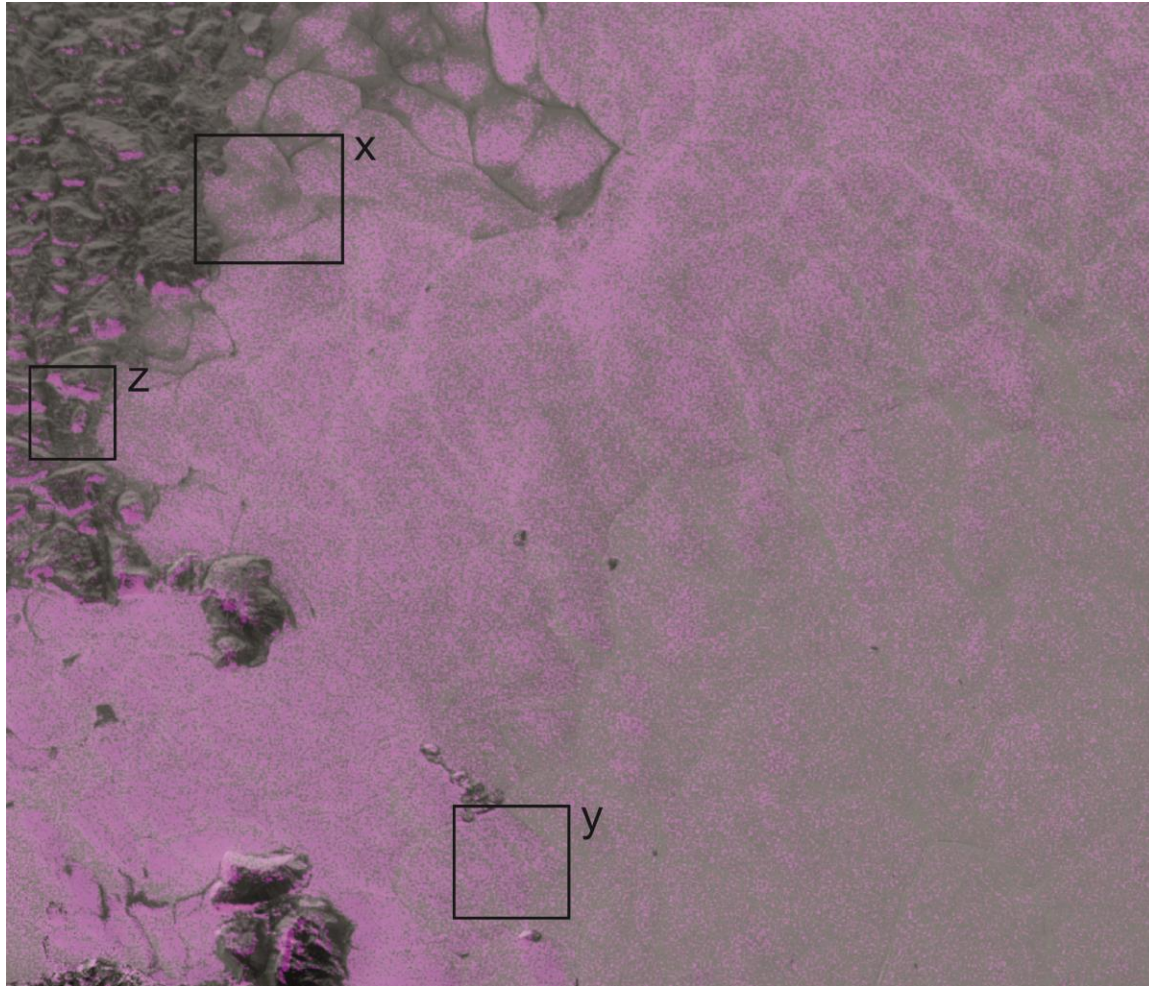
**Fig. S4**

Analysis of MVIC data using a CH$_4$ filter, based on the 0.89 µm absorption band, reveals that the areas where dunes are well developed also show stronger CH$_4$ absorption (x). The extent of the image is indicated in Fig. S1. In addition, the wind streaks to the southeast of Colleta de Dados Colles (shown in Fig. 1E) are also highlighted as a strong CH$_4$ response (y). The strongest, although spatially isolated and discrete responses, however, are found in the mountains of AIM, and are likely to indicate frosts and thus, perhaps, a source of sediment for the dunes (e.g. z).

902
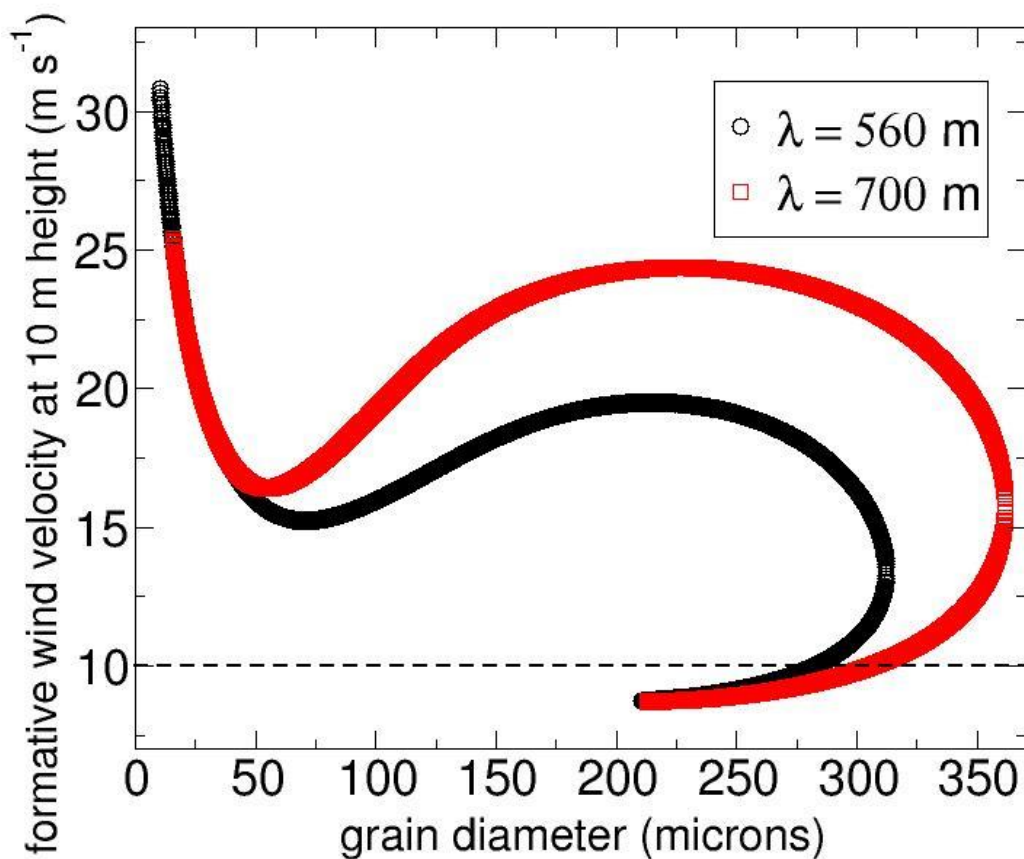
Fig. S5.

Possible pairs of grain size and wind velocity (at height of 10 m), which form transverse dunes with the observed values of spacing $\lambda = 560$ m and $\lambda = 700$ m under the atmospheric conditions valid for Pluto (*15*). The dashed line represents likely maximum wind speeds for Pluto (*16*).